Applied Energy 316 (2022) 119132

Contents lists available at ScienceDirect

Applied Energy

journal homepage: www.elsevier.com/locate/apenergy

Adaptive neural dynamic surface control for uniform energy exploitation of floating wind turbine

Jafar Keighobadi [a], Hadi Mohammadian KhalafAnsar [a,*], Peiman Naseradinmousavi [b]

[a] *Department of Mechanical Engineering, University of Tabriz, Tabriz, Iran*
[b] *Department of Mechanical Engineering, Sandiego State University, Sandiego, USA*

HIGHLIGHTS

- We updated the model of a floating wind turbine and ran simulations in the presence of disturbances.
- We describe a method for achieving stability of a floating wind turbine using dynamic surface control (DSC).
- Integral terminal sliding mode included in dynamic surfaces and raised-cosine RBFs to estimate the uncertainty upper bound.
- In the area of greater efficiency use, we employed LQR in comparison with RBFNN.
- Using Lyapunov-based analysis, we demonstrate the closed loop's stability as well as the tracking error's convergence.

ARTICLE INFO

Keywords:
Floating wind turbine
RBFNN
LQR
Adaptive control
Dynamic surface
Neural network

ABSTRACT

To avoid the harmful effects of global warming on the earth planet and its atmosphere, the expansion of wind energy consumption based on new control techniques leads to improved energy capacity. The development of wind power plants on the sea is more efficient owing to the stronger wind flows in comparison with the onshore structure. Furthermore, stable installation of the offshore wind energy base meets the energy management requirements of today's consumers. As a result, dependency on fossil fuels as the main source of global warming decreases. The feedback control system and on-line sensor signals provide the stability and increased efficiency of the floating wind turbine. The aggressive environment and large size structure of the turbine lead to entering uncertainty in the turbine model and exogenous noises that should not be effectively compensated by conventional control methods. Therefore, a radial based functional neural network (RBFNN) controller is proposed to estimate and compensate the effect of uncertainty on feedback control of the wind turbine. For comparison purposes, a linear quadratic regulator (LQR) state feedback is also developed for optimal control of the floating wind turbines. The neural network adaptively determines the upper bound of uncertainty/noise. Therefore, conservative high-gain control actions to achieve robustness of the classical feedback controllers against structural deviations of the turbine body are decreased. In our newly proposed adaptive control algorithm, using a basic raised cosine function guides to restore the computational efficiency of RBFNN. With the Lyapunov-based stability analysis, the final limits of the closed-loop system and the convergence caused by the terminal sliding mode (TSM) tracking error are determined. Detailed software simulations of both the LQR and the designed RBFNN control systems indicate the superiority of the neural network-based approach.

1. Introduction

Accelerated energy consumption of today's life results in abnormal global warming because of inevitable applications of fossil fuels. Specialists all around the world try to increase the facility of renewable energy. For example, in the interval 2007–2013, the United States experienced an annual average 7.1 GW increase in wind power capacity. By continuing this procedure over the next ten years, approximately 40% of the whole country's electricity could be provided via wind power [1]. Besides, wind turbines in offshore environments are exposed to

* Corresponding author.
E-mail addresses: Keighobadi@tabrizu.ac.ir (J. Keighobadi), H_Mohammadian96@ms.tabrizu.ac.ir (H. Mohammadian KhalafAnsar), pnaseradinmousavi@sdsu.edu (P. Naseradinmousavi).

https://doi.org/10.1016/j.apenergy.2022.119132
Received 28 August 2021; Received in revised form 17 March 2022; Accepted 13 April 2022

large platform motions, which may cause fatigue loading and shortened life, in addition to harmful power fluctuations. To decrease the destructive phenomena effects, the development of advanced multi-aim control schemes for rejection of disturbances and maximization of capturable power is considered. Although modeling uncertainties are partly compensated through feedback control actions in achieving the sustainable energy aim, a complete modeling of wave disturbances is unavoidable to decrease control actuator burden and saturation issue.

The significance of feedback-based optimization of the captured power arises mostly owing to the insertion of the turbine in a region under wind anomaly. The oscillation of wind power owing to wave and wind disturbances on the predicted power observation is attenuated through the design and implementation of the combined feedback control strategy. Hereupon, S. Christiansen et al. have implemented a simplified model of the turbine to estimate the total captured power through a feedback control system [2]. However, in the proposed feedback control mechanism, stabilization of the nacelle yaw angle was not declared. Through an advanced model-based control, both the relative motion of the turbine and nacelle yaw angle may be managed to further optimization of wind farm output. Besides, several studies have shown that improved control techniques can significantly extend the fatigue life of the floating wind turbine in deep water with minimal cost or even with decisive consequences for energy amount. For example, compared with a basic proportional-integral gain controller, a multi-objective LQR controller proposed in [3] can decrease height of platform about 18% without affecting on the energy capture. As significant wind and wave disturbances surge floating wind turbines, controllers with capability in predicting and managing such disturbances should be considered. According to some recent researches, compared with a baseline controller, implementation of wind turbulence estimation in the control system yields a tower lateral fatigue load by 38% and power value by 44% as well [2]. In an efficient active feedback controller, the designer should enter exogenous noise/disturbance information in the control process. In documented research works, linear noise matrix was commonly configured in proposed modeling methods. Offshore floating wind turbine management focuses on multi-objective control with disturbance handling based on effective mathematical modeling. Furthermore, mathematical modeling of intricate dynamics leads to time-consuming manipulation of the successful management of a floating wind turbine due to the movements of a floating platform and the flexibility of designs. In this study, we suggest a mix of traditional robust controllers, such as sliding mode control, and intelligent controllers of the neural network type to meet the robust and tracking requirements of the wind turbine control system. Different actuators are used for supplementary functions such as managing stage onrush and transmission loads, in addition to increasing power capacity. In addition, Ni et al. suggested a neuro-control approach for semi-dynamic vibration management of stay links using magnetorheological dampers in the realm of learning controllers [4]. Shiraishi et al. have proposed a flexible neural structure to control a three-story main model with a model damper, and they were able to achieve a good control goal arrangement [5].

Dynamic surface control (DSC) is a systematic design method for the control of nonlinear systems that are unpredictable [6–8]. It addresses the tracking control issue by defining coordinates, as well as tracking error and auxiliary control variables. The incorporation of appropriate integral terms into DSC error surfaces improves steady-state tracking and robustness [9–10]. For high-precision, finite-time, and resilient dynamic system control, terminal sliding mode (TSM) has been applied in a variety of applications [11–13]. Researchers have piqued interest in TSM's benefits in mechanical systems. For robust and finite-time control of stiff manipulators, non-singular and continuous kinds of TSM have been utilized. Some studies used TSM with fractional derivatives to increase the convergence speed of fully driven mechanical systems [14–16]. TSM enhances the standard sliding mode (SM) by using nonlinear switching surfaces, which results in finite-time sliding motion stability. For strong and time-consuming control of stiff manipulators, non-singular and continuous TSM types are utilized.

Artificial neural networks (NN) are strong tools for data aggregation, model categorization, optimization, and function approximation that are inspired by biological neurons. The NN approximation offers a viable basis for adaptive control of uncertain mechanical systems [17,18]. Sun et al. have applied Gaussian radial basis functions (RBF) to create an adaptive SM controller for robot operators, with adjusting capability to unmeasured matching speed [19]. Tran and Kang have combined radial basis function neural networks with TSM for finite-time adaptive control of robot operators [20]. Similarly, Zhou et al. have proposed adaptive RBFNN with back-stepping method [21]. Liu et al. suggested an adaptive NN controller with an appropriate hidden layer size for robots control in task space [22].

Based on the information provided by Homer [1], in this study, we created a simulation model of a floating wind turbine. Since the entire modeling of wind turbines encounters to leakages within perturbation dynamics, the suggested model in this work collects the impacts of wave and wind disturbances. As a result, it serves as a foundation for complete state-space modeling for the design of various control systems while wave and wind turbulence simulations are also carried out. The suggested RBFNN is utilized to estimate the unknown components of the dynamical system as part of the adaptive control rule. Along with the design procedure of the general structure of the control technique, the dynamic surface is specified, and the controller parameter is adaptively adjusted through the Lyapunov stability analysis. The wind turbine's stability and the decrease of tracking error to zero as the desired performance are obtained through utilizing this control rule. Additionally, the effects of waves and wind disturbances are eliminated using the neural network. Another purpose of the control system in the floating wind turbines is to maintain a steady amount of energy and stable circumstances. As the main innovation, the adaptive feedback controlling by combination of RBFNN with dynamic surface controllers, allows the wind turbine to reach stable conditions under stiff situations, resulting in uniform energy production. The following is how the rest of the article is arranged. The floating wind turbine's core mathematical concept is explained in Section 2. The suggested controllers' architecture and convergence analysis are discussed in Section 3. Section 4 shows the findings of Matlab-based comparison software simulations. Section 5 brings this paper to a conclusion.

2. Wind turbine model

The research on the floating wind turbines is based on a model developed by the National Renewable Energy Laboratory in the United States. The present turbine concept comprises three triangular floating cylinders and a center cylinder that controls the tower. The structure weighs 13.5 kT and sits at a depth of 13.46 m below sea level. The forces operating on the system, such as buoyancy force, drag force, air thrust, drag force, and cable drag force, are computed analytically for modeling.

2.1. Buoyancy force

According to Archimedes' principle, the buoyancy force acting on an item is equal to the weight of the fluid being moved by the object. The effective buoyancy force on the i-th floating cylinder is [1]:

$$\overrightarrow{F}_{B,i}(x) = \rho_{\omega} g A_i l_i \widehat{e}_3, i = 1:12 \tag{1}$$

where ρ_{ω} denotes the density of water, g the gravity constant, A_i the cross-section of the cylinder, l_i the length of cylinder and $\widehat{e}_3$ the unity vector along z-axis. For the highest floating cylinders, the center of buoyancy will change as:

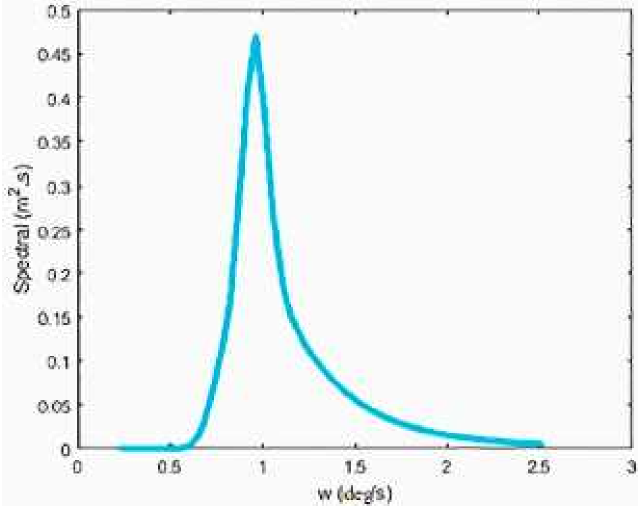

Fig. 1. *JONSWAP* spectrum.

$$l_i(x_g,\theta) = \frac{l_{0,i}}{2} - w_{h,i} - [\theta_y \theta_x 1] r^b_{gi,0} \tag{2}$$

where $r^b_{gi,0}$ is a fixed vector indicating the floating wind turbine center of mass with respect to the cylinder's initial center of mass, and consider $w_{h,i}$, θ_y, θ_x representing height from center of mass of the cylinder to the surface of water, rotating angles around y-axis and x-axis, respectively. Each base with three cylinders includes forces, as follows:

$$\begin{aligned} F_{i_a} &= A_{i_a} l_a g \hat{e}_3 \\ F_{i_b} &= A_{i_b} l_b g \hat{e}_3 \\ F_{i_c} &= A_{i_c} l_i(x_g,\theta) g \hat{e}_3 \end{aligned} \tag{3}$$

With A_i indicating cross-section of cylinders. When the computed forces in eq. (3) are multiplied by the appropriate effective length of arms, the torques are:

$$\begin{aligned} T_{i_a}(x) &= R r^b_{a_{gi}} \times F_{i_a} \\ T_{i_b}(x) &= R r^b_{b_{gi}} \times F_{i_b} \\ T_{i_c}(x) &= R r^b_{c_{gi}} \times F_{i_c} \end{aligned} \tag{4}$$

In eq. (4), r^b_{gi} denotes the distance between the centers of mass of turbine and cylinders, and R defines a transformation matrix as follows.

$$\mathrm{R} = \begin{bmatrix} 1 & -\theta_z & \theta_y \\ \theta_z & 1 & -\theta_x \\ -\theta_y & \theta_x & 1 \end{bmatrix} \tag{5}$$

The three rotation angles $(\theta_x, \theta_y, \theta_z)$ in radian are triple orientation states of the wind turbine. Finally, the gravity force acting on the center of mass of the turbine is obtained:

$$\vec{F}_G = -m_g g \hat{e}_3 \tag{6}$$

With m_g as the total mass of the turbine. Since the general gravity force passes through the center of mass, there exists no gravitational torque. The total force and torque are obtained by adding the gravity in eq. (6) on the buoyancy force components in eq. (1), respectively as:

$$\begin{aligned} \vec{F}_B(x) &= \sum_{i=1:12} \vec{F}_{B,i} + \vec{F}_G \\ \vec{T}_B(x) &= \sum_{i=1:12} \vec{T}_{B,i} \end{aligned} \tag{7}$$

2.1.1. Wave model

According to the linear wave theorem, a regular sinusoidal waveform with a height of 1.75 m and a spectral period of 12 s is defined as [1]:

$$h\left(\vec{x}_w, t, \alpha\right) = A\sin\left(\zeta\left(\vec{x}_w, t, \alpha\right)\right) \tag{8}$$

where A, t, α and $\vec{x}_w$ represent the wave height's amplitude, processing time, change in direction around the vertical z-axis, and spatial location of the wave height, respectively. Finally, the parameter ζ is calculated as follows.

$$\zeta\left(\vec{x}_w, t, \alpha\right) = \frac{-\omega^2}{g}\left(\hat{e}_1 R_z^T(\alpha)\vec{x}_w\right) + \omega t + \varphi \tag{9}$$

In which ω, g, $\hat{e}_1$, R_z^T, and φ stand for the wave frequency, gravity acceleration, unity vector along x-axis, transpose of transformation matrix R_z around the z-axis and phase angle, respectively. The corresponding R_z^T is defined as:

$$R_z = \begin{bmatrix} \cos(\alpha\pi/180) & -\sin(\alpha\pi/180) & 0 \\ \sin(\alpha\pi/180) & \cos(\alpha\pi/180) & 0 \\ 0 & 0 & 1 \end{bmatrix} \tag{10}$$

The *JONSWAP* spectrum S_{nn} is developed according to the Pierson–Moskowitz spectrum $S_{nn}(\omega)_{p_M}$ which is characterizable in marine environment as:

$$S_{nn} = S_{nn}(\omega)_{p_M} \gamma_p \exp\left[\frac{(\omega-\omega_p)^2}{2\sigma^2\omega_p^2}\right] \tag{11}$$

where γ_p and *exp* stand for the peak increase factor, and exponential function, and σ the peak width of the spectra becomes:

$$\begin{aligned} \sigma &= 0.07 \quad \omega \le \omega_p \\ \sigma &= 0.09 \quad \omega > \omega_p \end{aligned} \tag{12}$$

In eq. (10), $S_{nn}(\omega)_{p_M}$ the *Pierson–Moskowitz* spectrum as:

$$S_{nn}(\omega)_{p_M} = \frac{H_s^2}{4\pi T_Z^4 \omega^5} \exp\left[\frac{1}{\pi T_Z^4 \omega^4}\right] \tag{13}$$

The design parameters H_s, T_z and ω are wave height, average periodic time and frequency, respectively. Now the amplitude in eq. (8) is computed as:

$$A = \sqrt{2S_{nn}\omega} \tag{14}$$

Fig. 1 shows the wave spectrum according to eq. (13). Now, referring to eq. (8) and substituting the amplitude, frequency and phase values, the value of h is fully determined. Hydrodynamic parameters, including velocity, acceleration and pressure, are computed as:

$$\begin{aligned} \vec{v} &= \omega e^{\left(\frac{-\omega^2}{g}z\right)} \begin{bmatrix} cos(\alpha)sin(\zeta) \\ sin(\alpha)sin(\zeta) \\ cos(\zeta) \end{bmatrix} \\ \vec{a} &= \omega^2 e^{\left(\frac{-\omega^2}{g}z\right)} \begin{bmatrix} cos(\alpha)cos(\zeta) \\ cos(\alpha)cos(\zeta) \\ -sin(\zeta) \end{bmatrix} \\ P_d &= \rho g e^{\left(\frac{-\omega^2}{g}z\right)} sin(\zeta), z = \hat{e}_3 R_z^T(a)\vec{x}_w \end{aligned} \tag{15}$$

2.2. Drag force

The drag force is a dissipating force resists to the relative motion between the body and fluid. For a transversely immersed cylinder, Morrison's equation provides a simple approximation of the surface drag force associated with direction of the flow [1]:

$$\vec{F}_{Dt,i} = K_{d,i}\left\|\vec{v}_{t,i}\right\| + K_{a,i}\vec{a}_{t,i} \tag{16}$$

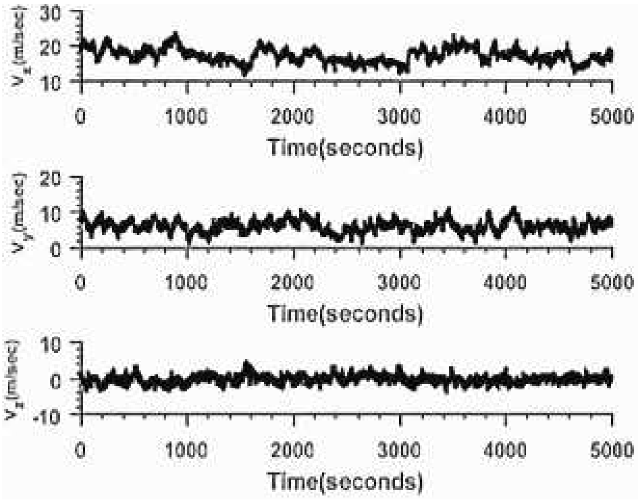

Fig. 2. Velocity of simulated wind along x, y and z directions.

where $K_{d,i}$ stands for the drag constant and $K_{a,i}$ stands for the inertia constant of Morrison equation. $\overrightarrow{v}_{t,i}$ and $\overrightarrow{a}_{t,i}$ are the transverse velocities and accelerations computed by:

$$\begin{aligned}\overrightarrow{v}_t &= R\begin{pmatrix}1&0&0\\0&1&0\\0&0&0\end{pmatrix}R^T\overrightarrow{\omega}_{rel}\\ \overrightarrow{a}_t &= R\begin{pmatrix}1&0&0\\0&1&0\\0&0&0\end{pmatrix}R^T\dot{\overrightarrow{\omega}}_{rel}\end{aligned} \tag{17}$$

the relative wave velocity, $\overrightarrow{\omega}_{rel}$, and its derivative will be obtained as:

$$\begin{aligned}\overrightarrow{\omega}_{rel} &= \overrightarrow{\omega} - \dot{\overrightarrow{x}}_g - \dot{R}\overrightarrow{r}^{b}_{gi}\\ \dot{\overrightarrow{\omega}}_{rel} &= \dot{\overrightarrow{\omega}}\end{aligned} \tag{18}$$

where $\overrightarrow{\omega}$ contains the first three components of the wave definition vector, $\dot{\overrightarrow{x}}_g$ consists of x, y, z components of the state variable vector, and $\dot{R}$ is derivative of the state transformation matrix defined by:

$$\dot{R} = \begin{bmatrix} & -\dot{\theta}_z & \dot{\theta}_y\\ \dot{\theta}_z & & -\dot{\theta}_x\\ -\dot{\theta}_y & \dot{\theta}_x & \end{bmatrix} \tag{19}$$

The drag and inertia constants in Morrison equation are given as:

$$\begin{aligned}K_{d,i} &= 0.5\rho D_{i,a}(i)C_{d,a}(i)len_a\\ K_{a,i} &= \frac{(1+C_a(i))\rho\pi D^2_{i,a}(i)len_a}{4}\end{aligned} \tag{20}$$

where $D_{i,a}$ stands for the diameter of the cylinder, $C_{d,a}(i)$ denotes the damping coefficient of the columns, len_a indicates the length of the cylinder and $C_a(i)$ refers to the coefficient of added mass for the cylinders. Considering the extra force created in the lowest floating cylinder due to the heave motion of the columns, the drag force is completed as follows [1].

$$\overrightarrow{F}_{Dh,i}(x,w) = K_{dh,i}\left\|\overrightarrow{v}_{h,i}\right\|\overrightarrow{v}_{h,i} + K_{ah,i}\overrightarrow{a}_{h,i} + P_iA_i\widehat{e}_h \tag{21}$$

In eq. (21), $K_{dh,i}$ and $K_{ah,i}$ express the drag coefficient and the constant coefficient of inertia in the heave plane, respectively. $\overrightarrow{v}_h$ and $\overrightarrow{a}_h$ show the equivalent heave velocity and acceleration vectors as:

$$\begin{aligned}\overrightarrow{v}_h &= R\begin{pmatrix}0&0&0\\0&0&0\\0&0&1\end{pmatrix}R^T\overrightarrow{w}_{rel}\\ \overrightarrow{a}_t &= R\begin{pmatrix}0&0&0\\0&0&0\\0&0&1\end{pmatrix}R^T\dot{\overrightarrow{\omega}}_{rel}\end{aligned} \tag{22}$$

$\widehat{e}_h$ denotes the transformed unity vector along z-axis as:

$$\widehat{e}_h = R\widehat{e}_3 \tag{23}$$

$K_{dh,i}$ and $K_{ah,i}$ should be computed separately as:

$$\begin{aligned}K_{dh,i} &= \frac{C_{dz}\rho\pi D^2_{i,a}(i)}{8}\\ K_{ah,i} &= \frac{C_{az}\rho\pi D^3_{i,a}(i)}{6}\end{aligned} \tag{24}$$

where C_{dz} and C_{az} stand for damping coefficient for heave plates and added mass coefficient for heave plates, respectively. The last term in eq. (21), P_iA_i should be calculated as:

$$F_p = P_iA_i = \left(\frac{\pi D^2_{i,a}}{4}\right)P(1) + \left(\frac{\pi D^2_{i,a}}{4} - \frac{\pi D^2_{i,b}}{4}\right)P(2) \tag{25}$$

where $P(1)$ and $P(2)$ stand for the elements of fluid pressure of the wave vector. Finally, the total force is obtainable for each column as:

$$\overrightarrow{F}_{D,i} = \overrightarrow{F}_{Dt,i} + \overrightarrow{F}_{Dh,i} \tag{26}$$

The torque associated with each force is computed using the linked coordinates of the column and the cross product of the torque arm and the distance between the turbine's center of mass and that of each cylinder. As a result, we need to use the transformation matrix as:

$$\overrightarrow{T}_{D,i}(x,w) = R\overrightarrow{r}^{b}_{gi} \times \overrightarrow{F}_{D,i} \tag{27}$$

2.3. Air thrust and drag force

The thrust force is in fact a component of wind force along the direction parallel to rotation axis of the rotor, while the drag force is the wind force component along motion direction of the blade. Although these forces permanently act on the entire blade surfaces, the resultant thrust force, $\overrightarrow{F}_A$ for all three blades is imposed at the thrust center point [1]:

$$\overrightarrow{F}_A = \frac{1}{2}\rho A_r C_t(\lambda,\beta)\left\|\overrightarrow{v}_n\right\|\overrightarrow{v}_n \tag{28}$$

where ρ and A_r show the air density and swept area of the rotor, respectively. The drift coefficient C_t is a function of the tip speed ratio λ and blade pitch angle β. The equivalent normal velocity onto the surface of the rotor blades, $\overrightarrow{v}_n$, is computable as:

$$\begin{aligned}\|\overrightarrow{v}_n\| &= [1\quad 0\quad 0]R^T_{eq}\overrightarrow{v}_{rel}\\ R_{eq} &= R_y(\theta_{tilt})R_z(\gamma)R\end{aligned} \tag{29}$$

with $\overrightarrow{v}_{rel}$ introduced by:

$$\overrightarrow{v}_{rel} = \overrightarrow{v} - \dot{\overrightarrow{x}}_g - \dot{R}R_z(\gamma)\left(\overrightarrow{r}_{gt} + R_y(\theta_{tilt})R_z(\theta_r)\overrightarrow{r}_{tc}\Big/2\right) \tag{30}$$

v is obtained from eq. (15) and the average wind speed is 18, 7 and 2 m/s in the directions x, y, z, respectively, as Fig. 2. In eq. (30) $\overrightarrow{r}_{gt}$ stands for distance vector from center of mass of the turbine to the center of thrust. $R_y(\theta_{tilt})$ demonstrates the transformation matrix around y-axis under, θ_{tilt}, the tilt angle of the rotor shaft with respect to the second axis

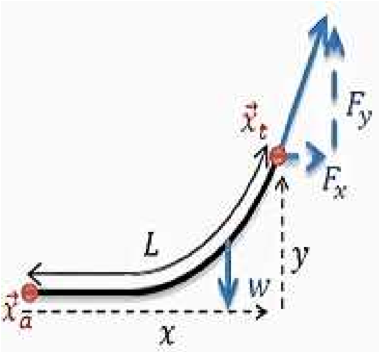

Fig. 3. 2-D Catenary line model [1].

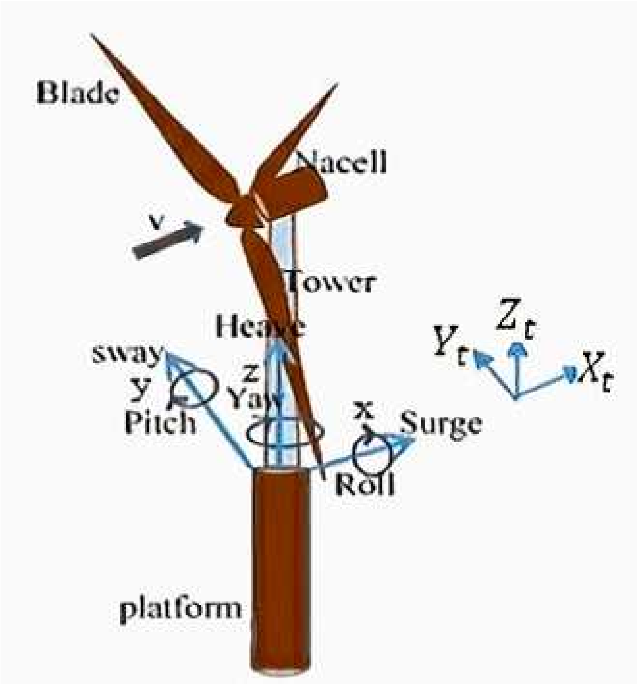

Fig. 4. Angular and displacement components of turbine.

of body frame,

$$R_y(\theta_{tilt}) = \begin{bmatrix} \cos(\theta_{tilt}\pi/180) & 0 & \sin(\theta_{tilt}\pi/180) \\ 0 & 1 & 0 \\ -\sin(\theta_{tilt}\pi/180) & 0 & \cos(\theta_{tilt}\pi/180) \end{bmatrix} \tag{31}$$

and $R_z(\theta_r)$ is the transformation matrix around z-axis with amount of θ_r, the azimuth angle of the rotor,

$$R_z(\theta_r) = \begin{bmatrix} 1 & 0 & 0 \\ 0 & \cos(\theta_r) & -\sin(\theta_r) \\ 0 & \sin(\theta_r) & \cos(\theta_r) \end{bmatrix} \tag{32}$$

In eq. (30) $\overrightarrow{r}_{tc}$ denotes center of thrust in body frame.

With N_{gr} as gear rate, we calculate its torque, with reappearing the same transformation matrices and aggregation of the generator torque term:

$$T = R \times \overrightarrow{F}_A + T_g R \frac{J_r + N_{gr} J_g}{J_r + N_{gr}^2 J_g} \hat{e}_1 \tag{33}$$

where T_g, J_r, J_g stand for generator torque, rotor inertia and generator inertia, respectively. The aerodynamic power is represented:

$$P = \frac{1}{2} \rho A_r C_p(\lambda, \beta) \| \overrightarrow{v}_n \|^3 \tag{34}$$

With C_p as the power coefficient. The torque balance about the rotor axis and the generator axis leads to [1]:

$$\begin{aligned} \dot{\overrightarrow{\omega}}_r &= \frac{1}{J_r} \left(\frac{P}{\omega_r} - k\left(\theta_r - \frac{1}{N_{gr}} \theta_g\right) - b\left(\omega_r - \frac{1}{N_{gr}} \omega_g\right)\right) \\ \dot{\overrightarrow{\omega}}_g &= \frac{1}{J_g} \left(-T_g + \frac{k}{N_{gr}} \left(\theta_r - \frac{1}{N_{gr}} \theta_g\right) + \frac{b}{N_{gr}} \left(\omega_r - \frac{1}{N_{gr}} \omega_g\right)\right) \end{aligned} \tag{35}$$

2.4. Drag force of cables

The mooring system consists a series of cables connecting the wind turbine to the seabed. The force cables provide a restoring force in response to the structural displacements caused by wind and wave disturbances. The Gaussian static model of a line is described in two dimensions. Hence, two nonlinear coupling equations relate the horizontal and vertical distances between the ends of the cable to the two-dimensional force at the connection point of the wind turbine. It is important to note that the equations change depending on whether a portion of the line rests on the sea bed, or whether it is fully ungrounded. Fig. 3 illustrates the force of the rope [1].

The vector $\overrightarrow{x}_{t,i}$ as the point of connection to the structure yields:

$$\overrightarrow{x}_{t,i} = \overrightarrow{x}_{a,i} - \overrightarrow{x}_g - R \overrightarrow{r}^b_{gci} \tag{36}$$

Decomposing the vector of $\overrightarrow{x}_{t,i}$ into its components along the axes gives:

$$\begin{aligned} \overrightarrow{x}_{th,i} &= \frac{\begin{pmatrix} 1 & 0 & 0 \\ 0 & 1 & 0 \\ 0 & 0 & 0 \end{pmatrix} \left(\overrightarrow{x}_{a,i} - \overrightarrow{x}_g - R \overrightarrow{r}^b_{gci} \right)}{\| \overrightarrow{x}_{t,i} \|} \\ y_t &= \begin{pmatrix} 0 \\ 0 \\ 1 \end{pmatrix} \left(\overrightarrow{x}_{a,i} - \overrightarrow{x}_g - R \overrightarrow{r}^b_{gci} \right) \end{aligned} \tag{37}$$

Using eq. (37), the forces in the x and y directions are obtained:

$$\begin{aligned} F_x &= \frac{W_c}{\left(1 \| \overrightarrow{x}_{t,i} \| \| \overrightarrow{x}_{t,i} \|^2 \| \overrightarrow{x}_{t,i} \|^3 \| \overrightarrow{x}_{t,i} \|^4 \| \overrightarrow{x}_{t,i} \|^5 \right) P_c \begin{bmatrix} 1 \\ y_t \end{bmatrix}} \overrightarrow{x}_{th,i} \\ F_y &= W_c \sqrt{\left(\frac{2}{\left(1 \| \overrightarrow{x}_{t,i} \| \| \overrightarrow{x}_{t,i} \|^2 \| \overrightarrow{x}_{t,i} \|^3 \| \overrightarrow{x}_{t,i} \|^4 \| \overrightarrow{x}_{t,i} \|^5 \right) P_c \begin{bmatrix} 1 \\ y_t \end{bmatrix}} + y_t \right) y_t} \begin{bmatrix} 0 \\ 0 \\ -1 \end{bmatrix} \end{aligned} \tag{38}$$

with W_c, P_c as the weight of rope and the 6 ×2 known coefficient matrix.

Our purpose from obtaining forces and torques is to represent the differential equation governing the plant:

$$f_Q(x, u, v, w) = \begin{bmatrix} \dot{\overrightarrow{x}}_g \\ \dot{\overrightarrow{\theta}} \\ \omega_r \\ \omega_g \\ \overrightarrow{f}_F(x, u, v, w) \\ \overrightarrow{f}_T(x, u, v, w) \\ f_Q(x, u, v) \end{bmatrix} \tag{39}$$

In eq. (39), $\overrightarrow{f}_F(\mathrm{x, u, v, w})$ will be the sum of all the forces acting on

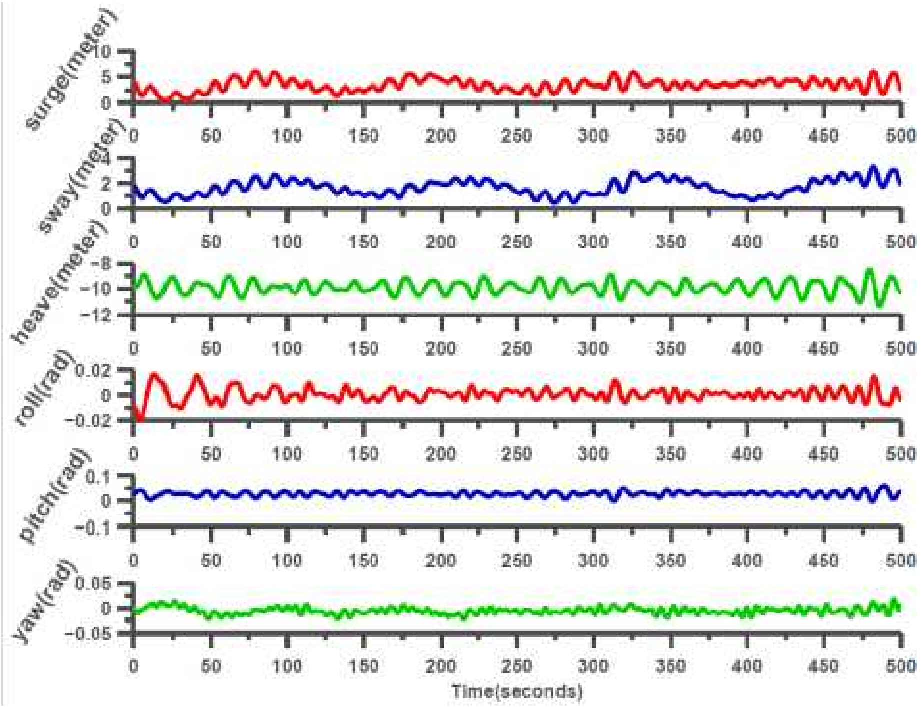

Fig. 5. Simulated states of floating wind turbine by MATLAB.

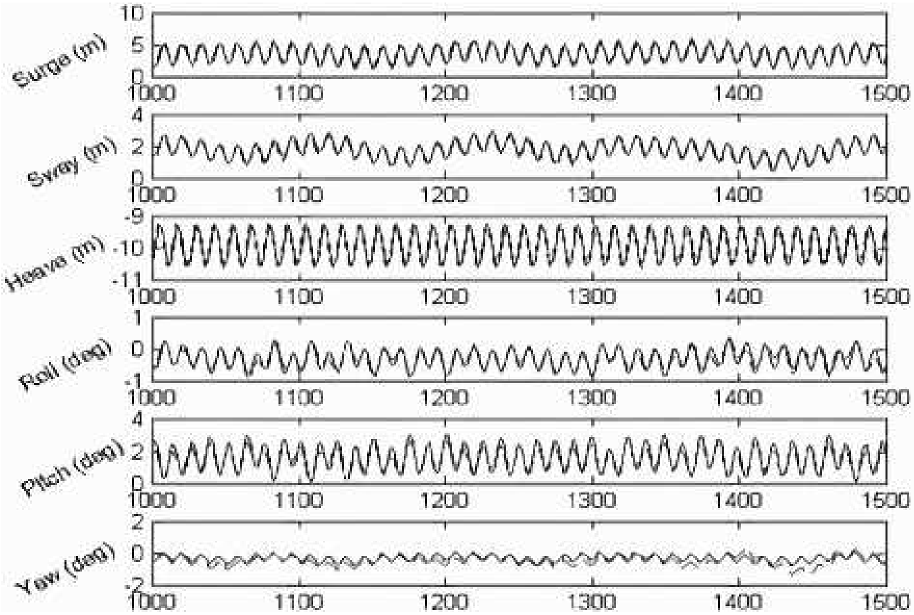

Fig. 6. Simulation of floating wind turbine state variables by Homer [1].

the structure:

$$\vec{f}_F(x,u,v,w) = \left(m_g I_{3\times3} + diag\left[\vec{m}_a\right]\right)^{-1} \sum_j \vec{F}_j(x,u,v,w) \tag{40}$$

where m_g shows the total weight of the structure, $I_{3\times3}$ a 3-dimensional identity matrix, $\vec{m}_a$ the mass, and $\vec{F}_j(\mathrm{x,u,v,w})$ will contain all applied forces.

The torque equation will be used to obtain angular accelerations, i.e., in eq. (39), $\vec{f}_T(\mathrm{x,u,v,w})$ will be the sum of all the moments resulting from the applied forces on the structure:

$$\vec{f}_T(x,u,v,w) = \left(RI_{g}^{-1}R^{T}\right)\sum_j \vec{T}_j(x,u,v,w) \tag{41}$$

where I_g is the inertial tensor around the vertical axis, R is the transformation matrix, and $\vec{T}_j(\mathrm{x,u,v,w})$ includes all of the torques by the forces acting on the structure. $f_Q(\mathrm{x,u,v})$ is also obtained as:

$$f_Q(\mathrm{x,u,v}) = \begin{bmatrix} \dot{\vec{\omega}}_r \\ \dot{\vec{\omega}}_g \end{bmatrix} \tag{42}$$

The aim of simulation is to determine the displacement components

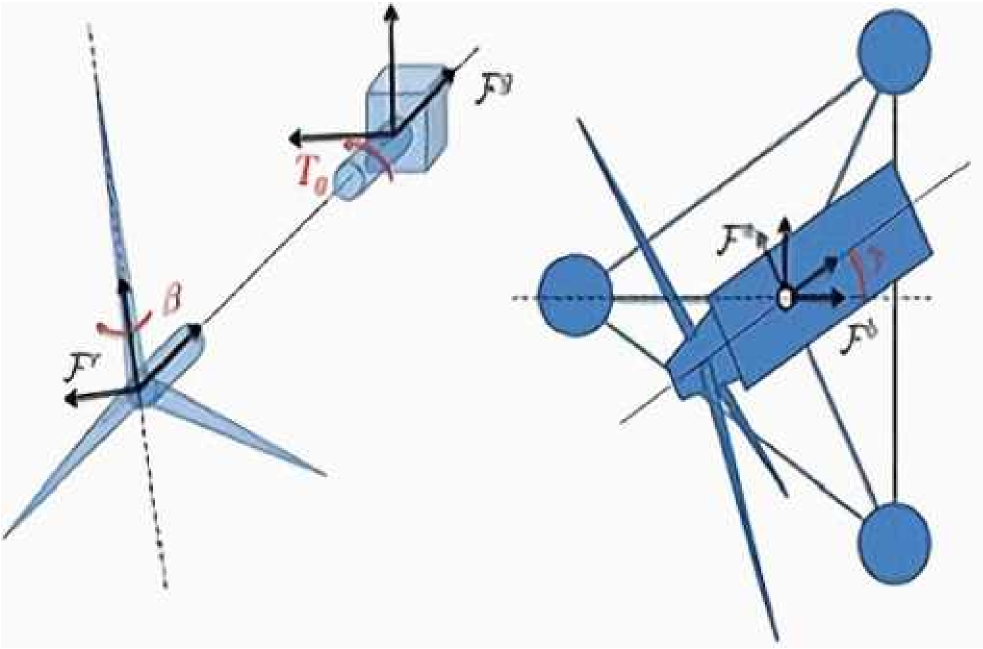

Fig. 7. Disturbance and control inputs.

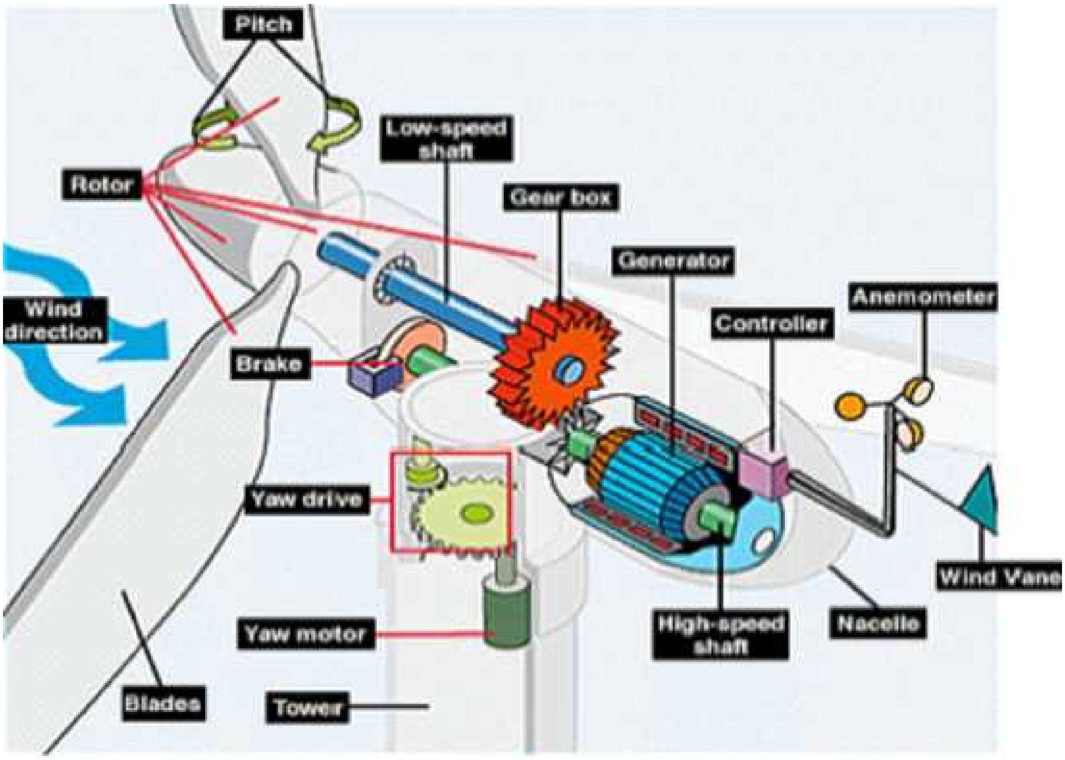

Fig. 8. Control system elements.

along the "X_t, Y_t, Z_t" directions, as "*surge, sway* and *heave*" respectively, and the angle components around body axes "x,y,z", as "*roll, yaw, pitch*", respectively. For becoming more familiar with the components of the problem, notice to the Fig. 4.

The important point in the simulation arises by the use of structure to store problem-solving data because of the large amount of information. Using the 4th order Runge Kutta solver, the simulation results in Fig. 5 are accurate according to simulated results of Homer model in Fast software as denoted in Fig. 6.

Incomplete available data including wave amplitude, wave frequency, drag coefficient and wind flow drifts guide to application of the approximated values in simulation of the Homer's model in particular owing to inaccessible source codes of Fast toolbox as a comparison reference. Therefore, according to experience and captured information in this research, the model of turbine system is improved to construct a full-information computational model for feedback control design purposes. Visual comparison of the model variables with the Fast model outputs confirms enough accuracy due to close upper and lower bounds

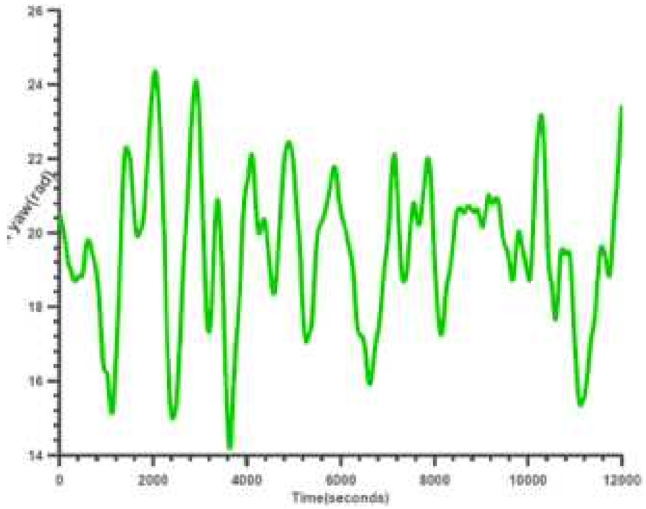

Fig. 9. Distribution of yaw angle as input.

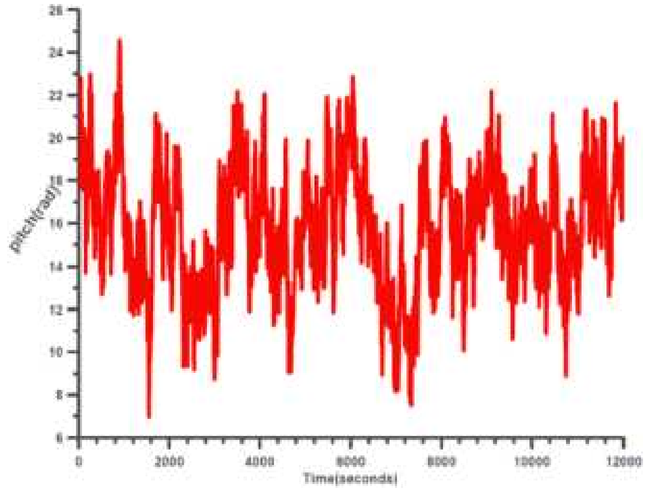

Fig. 10. Distribution of pitch angle as input.

and oscillations in state variables. Lack of fluctuation in bounds of states as other advantage of the developed model with regarding to the Homer's type and the system controllability satisfy us to apply various types of controllers to have a resembling comparison between output responses.

3. Control of desired states

Three control inputs determined for the wind turbine control system include total pitch angle β, generator torque T_g, and yaw angle as shown in Fig. 7. Fig. 8 depicts a schematic of control system configuration in which the generator torque is changed via the controller and the desired speed is accomplished by utilizing the shaft gearbox. The specific motor and driver will be utilized to modify the yaw angle as well.

Each blade revolves around an axis that runs the length of the blade. However, owing to encountering periodic fluctuation effects, advanced control techniques should be applied to hold the unified angle as the collective blade pitch angle while all of the blades spin simultaneously. In this study, we shall solely discuss collective blade pitch control for the sake of simplicity. Our simplified model for this rotation ignores actuator dynamics, resulting in an implausible capacity to adjust the angle instantly. In the nonlinear model, we may prevent such unrealistic motions by restricting the rate at which this angle can be shifted. We must also guarantee that the developed controllers conform to this restriction.

An electrical circuit incorporated within the generator can control the generator torque, while rotation angle sensors are required for the two input angles. Environmental circumstances may change quickly when wind turbines are in operation. In this research, through suggested controllers the design parameters are adjusted in such a way that the control inputs guide the state variables approach the original and intended conditions, i.e., the system converges to a stable desired condition and away from disturbance effects.

The angle between the unit vectors $\hat{e}_1^n$ and$\hat{e}_1^b$ in the body frame is known as the nacelle yaw angle which its actuator dynamics is neglected as the case of blade pitch angle. Through limiting the open-loop control input trajectories to those intended to replicate realistic reactions against the wind disturbance with the goal of easy power collection, similar to the 5 MW baseline controller, unrealistic rotations in the nonlinear model are prevented.

First, the yaw angle is produced within the objective of tracking the wind direction. However, owing to the limited speed of the yaw actuator, the one-to-one trajectory is smoothed using a locally weighted scatter plot smoothing method such that its maximum time derivative is less than the actuator limitation of 0.3 deg/s. The resulting yaw trajectory, overlaid on the wind direction, is shown in Fig. 9.

The blade pitch angle trajectory was then created with the goal of maintaining constant aerodynamic power. This is carried out by setting the instantaneous change in power to zero for all time, or as:

$$\delta P(t) = \frac{\partial P(t)}{\partial x}\delta x + \frac{\partial P(t)}{\partial u}\delta u + \frac{\partial P(t)}{\partial v}\delta v = 0 \tag{43}$$

where the power $P(t)$ is obtained from eq. (34). Due to the small variation of $P(t)$ with respect to state variables, by removing the state term, and inserting the relevant inputs, eq. (43) simplifies to.

$$\frac{\partial P(t)}{\partial \beta}\delta\beta + \frac{\partial P(t)}{\partial \gamma}\delta\gamma + \frac{\partial P(t)}{\partial v}\delta v = 0 \tag{44}$$

the value of β angle is obtained as the control goal:

$$\delta\beta = -\left(\frac{\partial P(t)}{\partial \gamma}\delta\gamma + \frac{\partial P(t)}{\partial v}\delta v\right) \Bigg/ \left(\frac{\partial P(t)}{\partial \beta}\right) \tag{45}$$

Therefore, solving this differential equation element-wise yields Fig. 10.

The last control input, generator torque is adjusted with changes in generator speed. In practice, the criterion for adjusting the generator torque is to keep the rotor speed constant:

$$\dot{\omega}_r = \frac{1}{J_r}\left(\frac{P}{\omega_r} - (N_{GR})T_g\right) = 0 \tag{46}$$

Which gives:

$$\delta T_g = \frac{1}{N_{GR}\omega_r}\left(\frac{\partial P(t)}{\partial \beta}\delta\beta + \frac{\partial P(t)}{\partial \gamma}\delta\gamma + \frac{\partial P(t)}{\partial v}\delta v\right) \tag{47}$$

The simulation result appears in the form of Fig. 11.

3.1. RBFNN control method

Dynamic surface controlling manages unpredictable nonlinear systems using a systematic design approach. Mainly, adding appropriate integral terms to the DSC error surfaces improves the steady-state tracking and resilience. Traditional SM theory is based on stabilizing a linear switching surface that lowers the order of the system dynamics; however, TSM evolves traditional SM by integrating nonlinear switching surfaces that result in finite sliding motion stability.

Artificial neural networks (ANNs) are powerful tools for data clustering, pattern classification, optimization, and approximation to universal functions [23,24]. In this case, Gaussian Radial Basis Functions

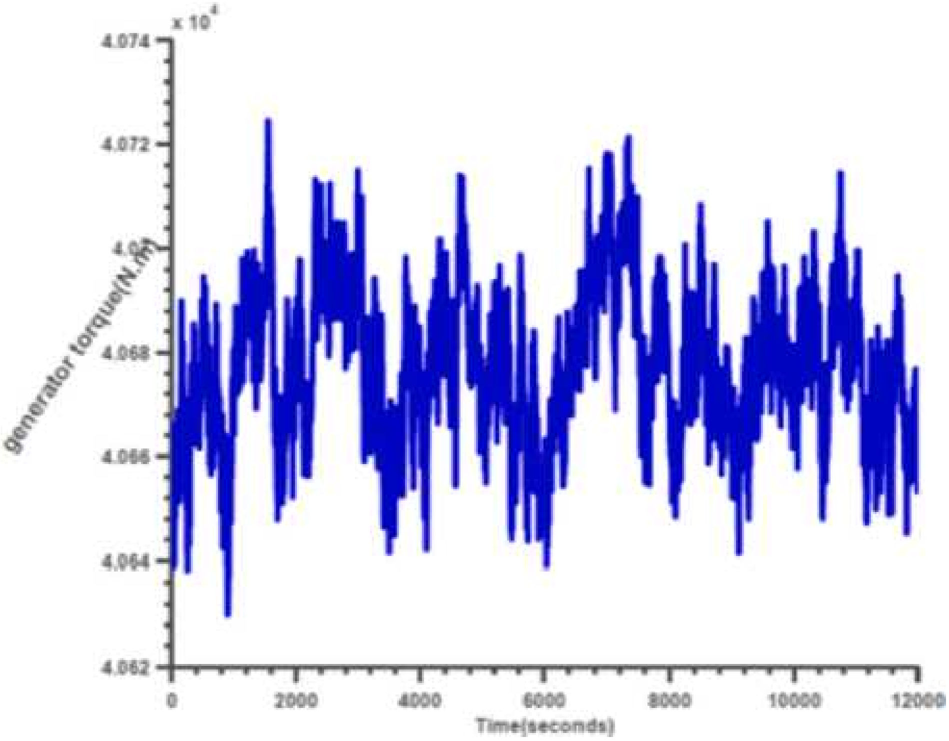

Fig. 11. Distribution of generator input torque.

(RBFs) are used to design an adaptive SM controller for blade pitch angle β, generator torque Tg, and nacelle yaw angle γ.

The main contribution of this paper is to present a new tracking controller for mechanical systems by combining the virtues of DSC, TSM and RBFNNs.

In a mechanical n-DOF system, whose configuration space is parameterized by the generalized coordinate's vector q ∈ R, Euler-Lagrange method results in the dynamical system equations as:

$$M(q)\ddot{q}+C(q,\dot{q})\dot{q}+D(\dot{q})+G(q)=u+\Delta(q,\dot{q},w) \tag{48}$$

where $M(q)$, $C(q,\ \dot{q})$, $D(\dot{q})$, $G(q)$, u *and* Δ are matrix/vector of inertia, Coriolis/centripetal, dissipative forces, gravitational terms, input force/torques, and the external disturbances/modelling uncertainties. The modelling uncertainties δ s are defined with respect to the corresponding nominal values subscripted with "0″ as:

$$\begin{aligned} M(q)&=M_0(q)+\delta M(q)\\ C(q,\dot{q})&=C_0(q,\dot{q})+\delta C(q,\dot{q})\\ D(\dot{q})&=D_0(\dot{q})+\delta D(\dot{q})\\ G(q)&=G_0(q)+\delta G(q) \end{aligned} \tag{49}$$

3.1.1. *Integral dynamic surface control*

To obtain the suitable dynamics of tracking errors, using the DSC formulation, we introduce the following tracking errors:

$$\begin{aligned} &e_1=q-q_d\\ &e_2=\dot{q}-v_d\\ &e_3=v_d-\varphi\\ &T\dot{v}_d+v_d=\varphi, v_d(0)=\varphi(0) \end{aligned} \tag{50}$$

with vector$e_1 \in \mathrm{R}^n$ standing for a direct measure of tracking performance; the intermediary tracking error $e_2 \in \mathrm{R}^n$ defined to enable a recursive control algorithm; $\phi \in \mathrm{R}^n$ denoting an auxiliary control vector; $v_d \in \mathrm{R}^n$ representing for low-pass filtered version of ϕ, $e_3 \in \mathrm{R}^n$ showing the filtering error, and $T \in \mathrm{R}^{n\times n}$ representing a positive definite matrix (PDM). To improve the robustness of DSC, in usage of SM surfaces, we further define the following integral error surfaces:

$$\begin{aligned} s_1&=e_1+\mathscr{I}(e_1,t)\\ s_2&=Hs_1+e_2\\ \mathscr{I}(e_1,t)&=\int_0^t \exp(-\lambda(t-\zeta))\psi(e_1(\zeta))d\zeta\\ \psi(e_1)&=\sum\nolimits_{i=1}^{3}L_i\tanh_\varepsilon^{a_i}(e_1) \end{aligned} \tag{51}$$

with $H \in \mathrm{R}^{n\times n}$ being a positive semidefinite coupling matrix; $\lambda > 0$, and $L_i \in \mathrm{R}^{n\times n}$, $i = 1$: 3, are diagonal PDMs; $0 < a_1 < 1$, $a_2 \geq 1$, $a_3 = 0$, $\varepsilon > 0$ and $\tanh_\varepsilon^{a_i}(e_1)$ is obtained by:

$$\tanh_\varepsilon^{a}(x)=\mathrm{col}\left(|x_i|^a\tanh\left(\frac{x_i}{\varepsilon}\right)\right)_{i=1}^{n} \tag{52}$$

The roles of different terms of the function $\psi(.)$ in convergence of the tracking error e_1 are as follows. The first $(0 < a_1 < 1)$ and the second $(a_2 > 1)$ produce large gains when e_1 is near and far from the origin, respectively. In the case $a_2 = 1$, the second term generates a uniform gain distribution. The last term $(a_3 = 0)$ is a robustifying term against bounded perturbations.

The DSC design is carried out by the following steps:

Step 1 (stabilization of s_1*).* We consider the following Lyapunov candidate and take its time derivative.

$$\begin{aligned} V_1&=\frac{1}{2}s_1^\top s_1\\ \dot{V}_1&=s_1^\top\Big(-Hs_1+s_2+e_3+\varphi-\dot{q}_d-\lambda\mathscr{I}(e_1,t)+\psi(e_1)\Big) \end{aligned} \tag{53}$$

According to the nonlinear damping, we obtain the auxiliary control input as.

$$\varphi\left(e_1,\dot{q}_d,t\right)=-K_1s_1+\lambda\mathscr{I}(e_1,t)-\psi(e_1)+\dot{q}_d \tag{54}$$

where $K_1 \in \mathrm{R}^{n\times n}$ is a design PDM. Hence, we have:

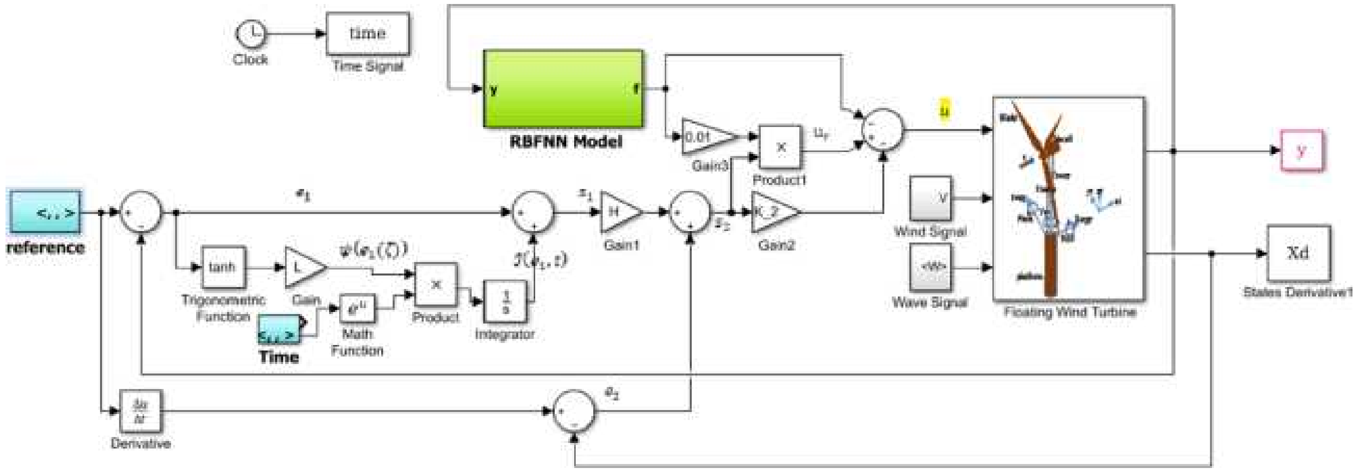

Fig. 12. Simulation graph of Floating Wind Turbine with Adaptive Surface Neural Network control in Matlab.

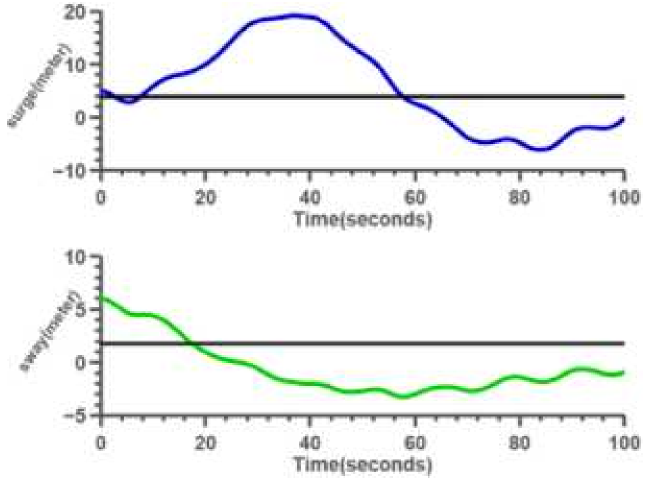

Fig. 13. Positions x and y through RBFNN control system.

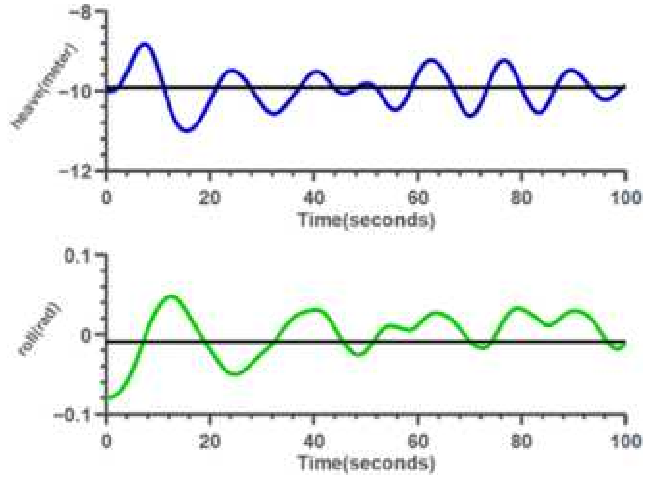

Fig. 14. Position z and Rotation around x of RBFNN system.

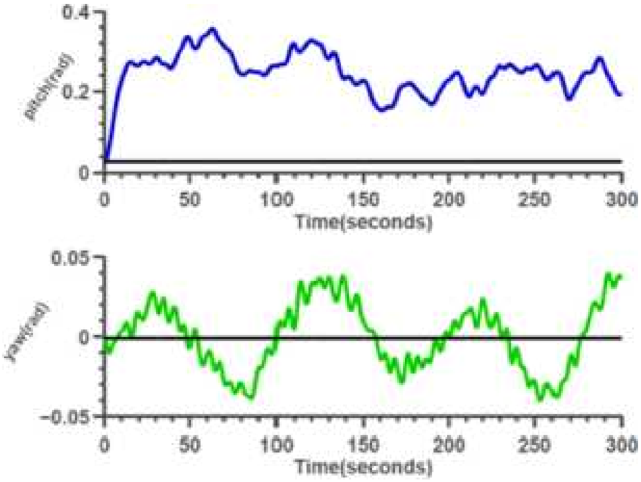

Fig. 15. Rotation around y and z through RBFNN system.

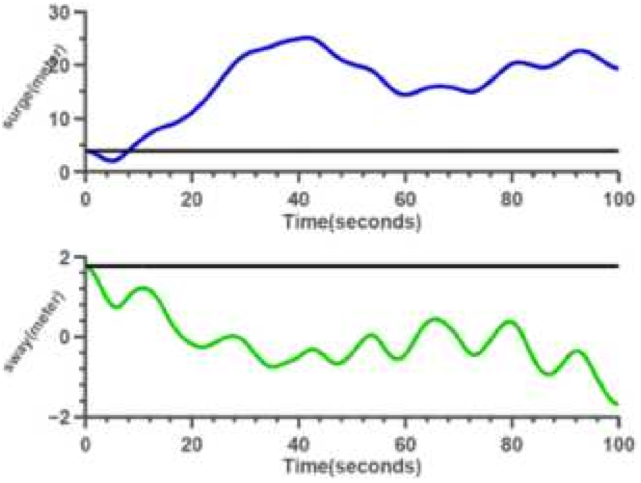

Fig. 16. Positions x and y through LQR system.

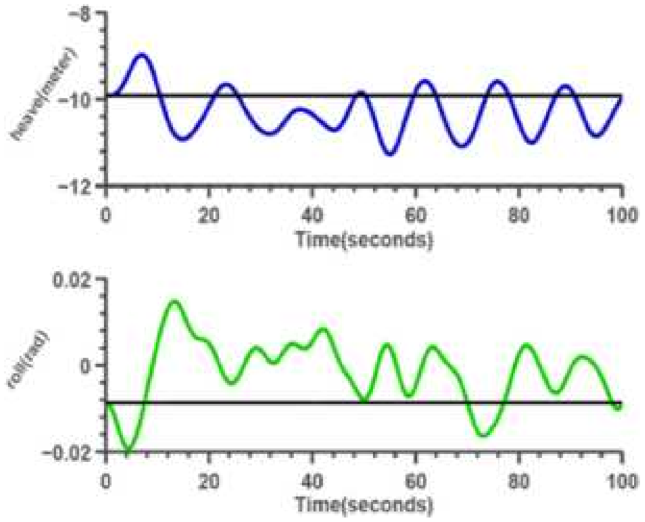

Fig. 17. Position z and angle around x through LQR system.

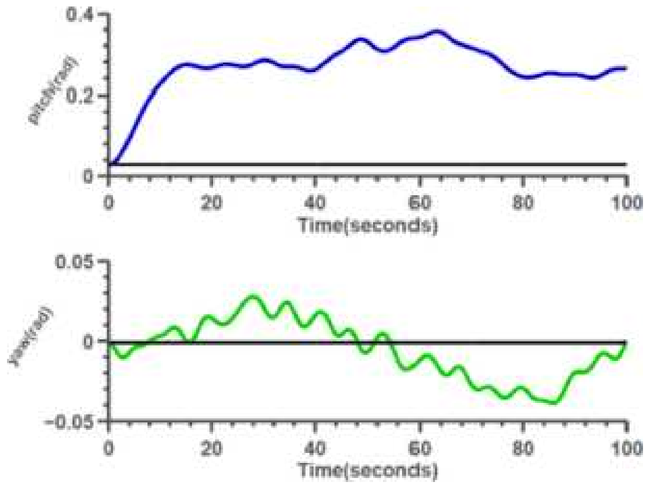

Fig. 18. Rotation angles around y and z through LQR controller.

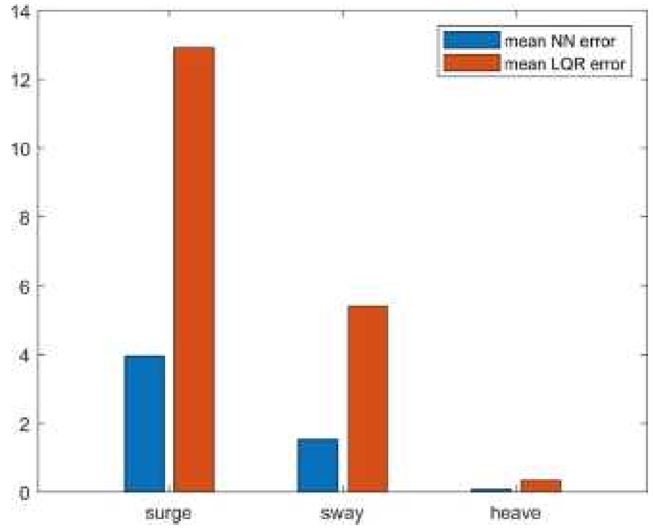

Fig. 19. Displacement error of RBFNN & LQR from reference model.

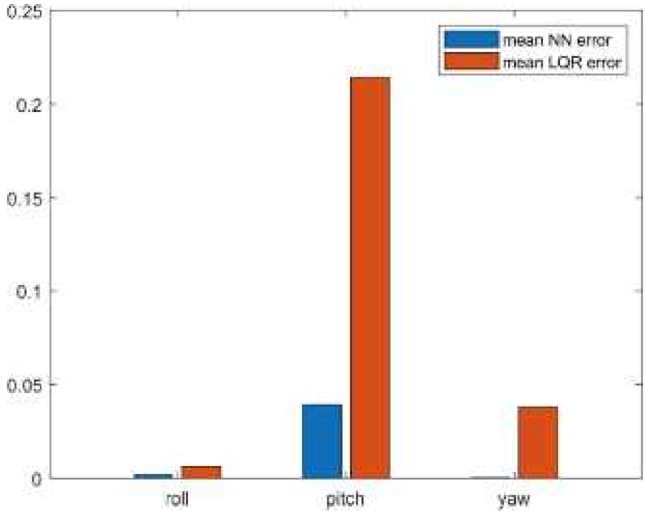

Fig. 20. Rotational error of RBFNN & LQR from reference model.

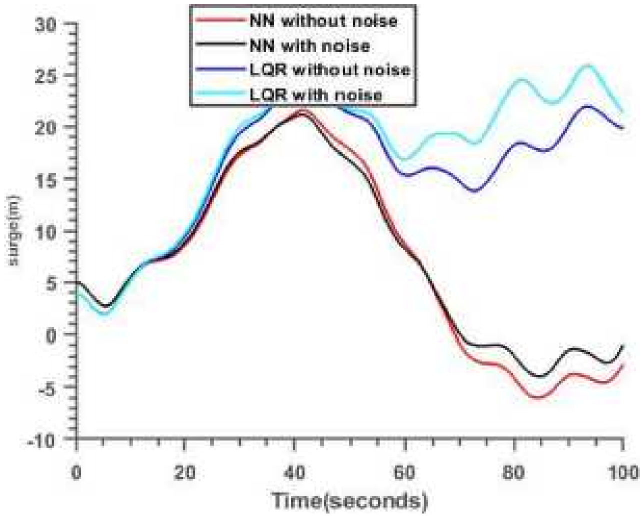

Fig. 21. Noise suppression performance of RBFNN & LQR on surge.

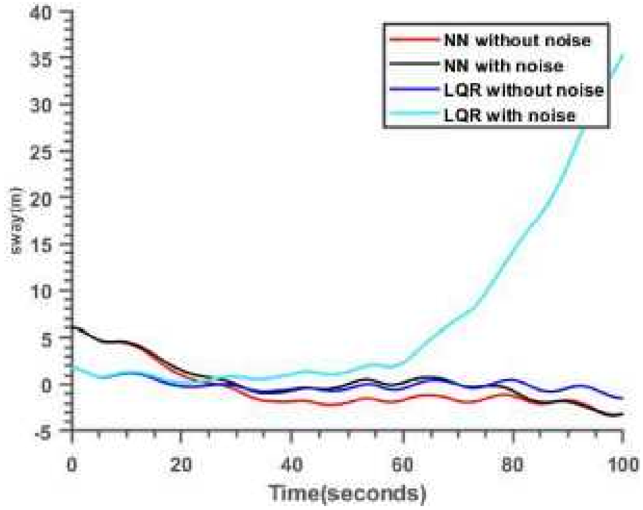

Fig. 22. Noise suppression performance of RBFNN & LQR on sway.

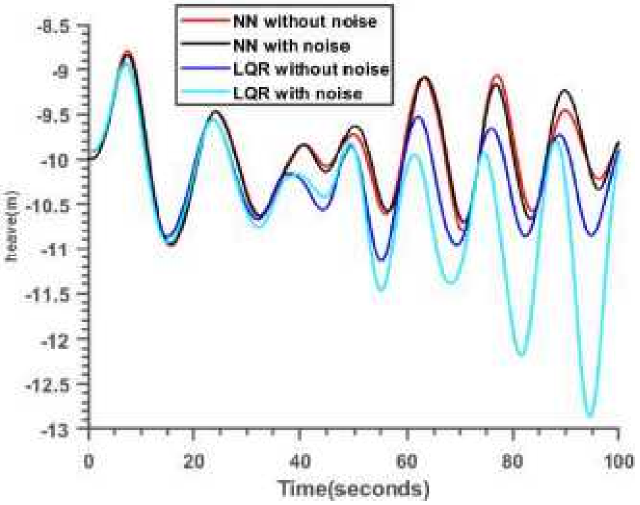

Fig. 23. Noise suppression performance of RBFNN & LQR on heave.

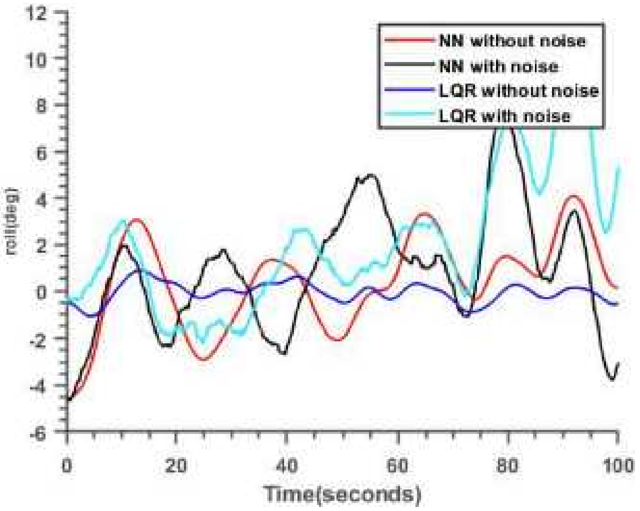

Fig. 24. Noise suppression performance of RBFNN & LQR on roll.

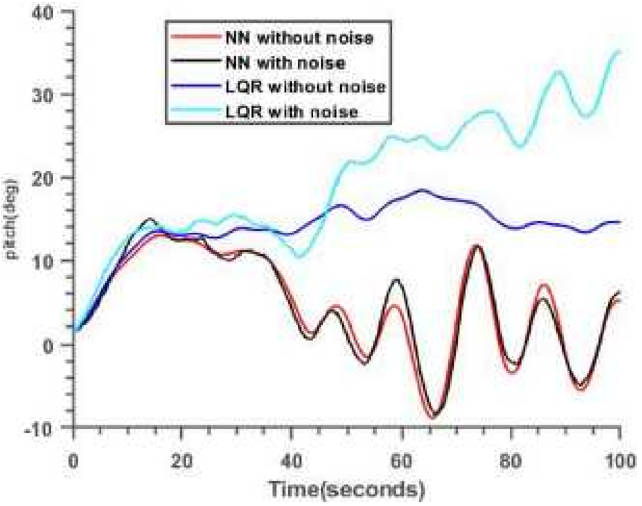

Fig. 25. Noise suppression performance of RBFNN & LQR on pitch.

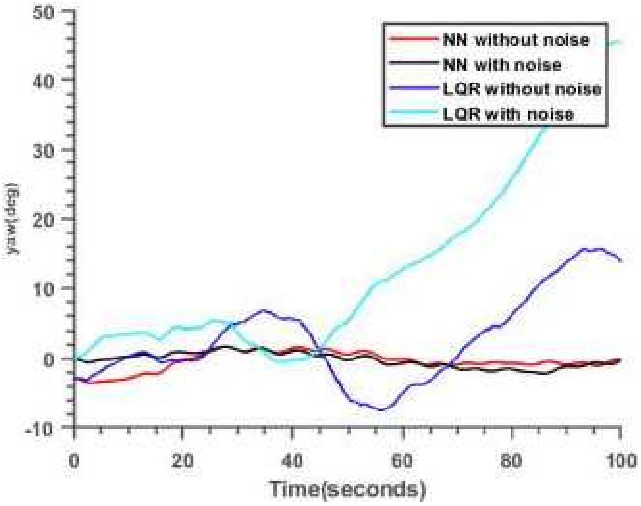

Fig. 26. Noise suppression performance of RBFNN & LQR on yaw.

$$\dot{V}_1 = -s_1^\top(H+K_1)s_1 + s_1^\top(s_2+e_3) \tag{55}$$

Step 2 (stabilization of s_2). Having Property 1 in mind, we consider the second Lyapunov function as:

$$\begin{aligned} V_2 &= V_1 + \frac{1}{2}s_2^\top M(q)s_2 \\ \dot{V}_2 &= -s_1^\top(H+K_1)s_1 + s_1^\top e_3 + s_2^\top(u+f+\delta f) \end{aligned} \tag{56}$$

where

$$\begin{aligned} f &= (I + C_0(q,\dot{q})H - M_0(q)H(H+K_1)\,)s_1 + M_0(q)Hs_2 \\ &+M_0(q)\left(T^{-1}+H\right)e_3 - D_0(\dot{q}) - G_0(q) - C_0(q,\dot{q})v_d\delta f \\ &= (\delta C(q,\dot{q})H - \delta M(q)H(H+K_1)\,)s_1 + \delta M(q)Hs_2 + \delta M(q)\left(T^{-1}+H\right)e_3 \\ &\quad - \delta D(\dot{q}) - \delta G(q) - \delta C(q,\dot{q})v_d + \Delta(q,\dot{q},w) \end{aligned} \tag{57}$$

Let.

$$u = -K_2s_2 - f + u_r \tag{58}$$

where the unknown function Δ (*q*, *q̇*, *w*) ∈ R^n accounts for the effects of unmodeled dynamics and external disturbances, $K_2 \in R^{n\times n}$ stands for a design PDM and $u_r \in R^n$ denotes a robust control term to be designed.

Substituting eq. (58) in eq. (56) leads to:

$$\dot{V}_2 = -s_1^\top(H+K_1)s_1 + s_1^\top e_3 - s_2^\top K_2 s_2 + s_2^\top(u_r+\delta f) \tag{59}$$

Step 3 (low-pass-filtering dynamics). The low-pass filtering error satisfies.

$$\dot{e}_3 = -T^{-1}e_3 - \ddot{q}_d + \eta(e_1,e_2,e_3,t) \tag{60}$$

where

$$\begin{aligned} \eta(e_1,e_2,e_3,t) = &\left(\lambda^2 I + \frac{\partial\psi(e_1)}{\partial e_1}\right)\mathscr{I}(e_1,t) - \left(\lambda I + \frac{\partial\psi(e_1)}{\partial e_1}\right)\psi(e_1) \\ &+\left(K_1 + \frac{\partial\psi(e_1)}{\partial e_1}\right)(-K_1e_1 - K_1\mathscr{I}(e_1,t) + e_2 + e_3\,)\# \end{aligned} \tag{61}$$

We consider the third Lyapunov candidate function as:

$$V_3 = V_2 + \frac{e_3^\top e_3}{2} \tag{62}$$

According to eqs. (60) through (62), the time derivative of V_3 satisfies the following inequality.

Table 1
Statistical specifications of tracking errors of adaptive RBFNN under noise compared with noise-free adaptive RBFNN and LQR.

State Variables	Optimal LQR without noise		Optimal LQR with noise		Adaptive RBFNN without noise		Adaptive RBFNN with Noise	
	Mean	*Standard Deviation*	*Mean*	*Standard Deviation*	*Mean*	*Standard Deviation*	*Mean*	*Standard Deviation*
Surge(m)	12.9240	10.0855	14.7300	10.6404	3.9583	6.1480	4.1251	6.5352
Sway(m)	5.4042	5.2373	5.5049	9.1461	1.5250	0.8258	1.9072	2.6220
Heave(m)	0.3343	0.3060	0.6502	0.7002	0.0798	0.2226	0.0943	0.1962
Roll(deg)	0.3552	2.1944	2.0225	2.9565	0.0974	0.2750	0.2693	1.6616
Pitch(deg)	12.2728	6.5317	18.0711	7.7349	2.2460	3.3346	3.100	4.3456
Yaw(deg)	6.5317	8.1131	13.4989	13.6650	6.3170	7.1310	6.4140	7.7854

$$\begin{aligned}\dot{V}_3 \leq -s_1^\top(H+K_1)s_1 + s_1^\top e_3 - s_2^\top K_2 s_2 + s_2^\top(\overline{u}_r + \delta f) - e_3^\top T^{-1} e_3 \\ -e_3^\top \ddot{q}_d + e_3^\top \eta(e_1,e_2,e_3,t)\end{aligned} \# \tag{63}$$

Step 4 (NN approximation). Now, we use NN approximation to compensate the uncertain term, δf. In this regard. We assume that $(q,\dot{q}) \in \Omega$ with $\Omega \subset \mathbb{R}^{2n}$ being a compact set. To ensure the feasibility of the tracking control problem, we further assume that the desired trajectory $q_d(.)$ is feasible in the set Ω, that is, $\Omega_d \subseteqq \Omega$.

Proposition 1. *There exists a positive continuous function* $\varrho : \mathbb{R}^{4n} \to \mathbb{R}^+$ *such that the following inequality holds globally:*

$$||\delta f|| \leq \varrho\left(q,\dot{q},q_d,\dot{q}_d\right) \tag{64}$$

Proof. For any $r \in \mathbb{R}^+$, let $\overline{\psi}(r) = \max_{||e_1|| \leq r}||\psi(e_1)||$. According to eq. (51), we have the inequalities.

$$\begin{aligned}||s_1|| &\leq ||e_1|| + \frac{\overline{\psi}(||e_1||)}{\lambda} \\ ||s_2|| &\leq ||He_1|| + ||e_2|| \\ ||\varphi\left(e_1,\dot{q}_d,t\right)|| &\leq ||K_1 s_1|| + 2\overline{\psi}(||e_1||) + ||\dot{q}_d||\end{aligned} \tag{65}$$

The low-pass-filtering state, v_d satisfies the following bound for all $t \in \mathbb{R}^+$:

$$\begin{aligned}||v_d(t)|| &\leq exp\left(\frac{-t}{\lambda_{max}(T)}\right)||\varphi\left(e_1(0),\dot{q}_d(0),0\right)|| \\ &+\lambda_{max}(T)\left(1 - exp\left(\frac{-t}{\lambda_{max}(T)}\right)\right)\sup_{0 \leq \varsigma \leq t}||\varphi\left(e_1(\varsigma),\dot{q}_d(\varsigma),\varsigma\right)||\#\end{aligned} \tag{66}$$

Taking the inequalities eq. (65) into consideration, the existence of the function $\varrho(.)$ is deduced from the assumption and the triangular inequalities of norm leads to:

$$\begin{aligned}||e_1|| &\leq ||q|| + ||q_d|| \\ ||e_2|| &\leq ||\dot{q}|| + ||v_d|| \\ ||e_3|| &\leq ||v_d|| + ||\varphi||\end{aligned} \tag{67}$$

By Defining:

$$\rho\left(q,\dot{q},q_d,\dot{q}_d\right) = \varrho^2\left(q,\dot{q},q_d,\dot{q}_d\right) \tag{68}$$

Imposing the Young's inequality and Proposition 1 gives:

$$s_2^\top \delta f \leq \frac{||s_2||^2 \rho\left(q,\dot{q},q_d,\dot{q}_d\right)}{2\epsilon} + \frac{\epsilon}{2} \tag{69}$$

for any positive ϵ. Over the set $\Omega \times \Omega_d$, for some positive ζ. we consider the RBFNN approximation as:

$$\rho\left(q,\dot{q},q_d,\dot{q}_d\right) = \theta^{*\top}\phi(\chi) + \zeta^*(\chi) \tag{70}$$

with $\chi = \mathrm{col}\left(q,\dot{q},q_d,\dot{q}_d\right)$; $\sup_{\chi \in \Omega}\Omega_d|\zeta^*(\chi)| \leq \zeta$. and an ideal weight vector $\theta^* \in \mathbb{R}^N$. Let $\theta \in \mathbb{R}^N$ be an estimate of θ^* by define $\widetilde{\theta} := \theta^* - \theta$. and considering the candidate Lyapunov function as:

$$V_4 = V_3 + \frac{1}{2}\widetilde{\theta}^\top \Gamma^{-1}\widetilde{\theta} \tag{71}$$

where $\Gamma \in \mathbb{R}^{n \times n}$ is a PDM. Applying the *NN* approximation (70) and using the nonlinear damping, we set the robust control input to.

$$\mathrm{u}_r = -\frac{(\theta^\top \phi(\chi) + \kappa)}{2\epsilon}s_2 \tag{72}$$

where $\kappa \geq \zeta$ is a design positive gain. Thereby, we obtain:

$$\begin{aligned}\dot{V}_4 \leq \quad & -s_1^\top(H+K_1)s_1 + s_1^\top e_3 - s_2^\top K_2 s_2 + \frac{(\zeta - \kappa)}{2\epsilon}s_2^\top s_2 - e_3^\top T^{-1} e_3 \\ & -e_3^\top \ddot{q}_d + e_3^\top \eta(e_1,e_2,e_3,t) + \frac{\epsilon}{2} + \widetilde{\theta}^\top\left(\frac{\phi(\chi)}{2\epsilon}||s_2||^2 + \Gamma^{-1}\dot{\widetilde{\theta}}\right)\end{aligned} \tag{73}$$

According to the last term in the right-hand side of (74), we select the NN update law as.

$$\dot{\theta} = \Gamma\left(\frac{\phi(\chi)}{\epsilon}||s_2||^2 - \gamma\theta\right) \tag{74}$$

where γ is a design positive scalar. Now we consider an RBFNN with the input $x = \mathrm{col}\,(x_j)_{j=1}^n \in \mathrm{R}^n$, a hidden layer composed of N neurons, and a single output. The output of the network is given by the nonlinear mapping $\theta^T\varphi(x)$ where $\theta \in \mathrm{R}^N$ is the weight vector and $\varphi\,(.) \in \mathrm{R}^N$ is the vector of basis functions. Using raised-cosine functions, the basis vector is defined as $\varphi(x) = \mathrm{col}\,(\varphi_j)_{j=1}^N$ where:

$$\begin{aligned}\phi_i(x) &= \prod\nolimits_{j=1}^n \phi_c\left(\frac{x_j - c_{ij}}{\sigma_{ij}}\right), i = 1:N \\ \phi_c(z) &= \begin{cases}\cos^2\left(\frac{\pi z}{2}\right), & \text{for}|z| \leq 1 \\ 0, & \text{elsewhere}\end{cases}\end{aligned} \tag{75}$$

The parameters $c_{ij} \in \mathrm{R}$ and σ_{ij} determine the position of the center and the width of the ij-th raised-cosine function, respectively. The compact support of the i-th basis function is $\prod_{j=1}^n\left[c_{ij} - \sigma_{ij}, c_{ij} + \sigma_{ij}\right]$. The implementation details of the designed RBFNN control system are depicted in Fig. 12, and the simulation results are shown in Figs. 13 through 15. Because of approximation of uncertainty and disturbance impact, we should highlight that the use of concise RBFNN makes our nonlinear controller simple for real-time execution. The control system of newly added Fig. 12 even inside the heavy Matlab Simulink is performed at 100 Hz within a Core i5 PC. According to our experiences with C++ based implementation on Linux Beagle-Bone board, this control system could be implemented about 200 Hz real-time.

3.2. LQR controller

Optimal control refers to a set of methods that search for the best possible solutions according to a performance index. As the main purpose, the optimal control determines actuator signals as inputs of the plant process to satisfy some constraints along with extremization of the selected performance index or cost function.

To obtain the following equilibrium point, the right side of state variables eq. (39) is set equal to zero:

$$\begin{aligned} x = \{&3.90m, 1.76m, -9.91m \\ &-0.50^{\circ}, 1.60^{\circ}, -0.00^{\circ} \\ &\quad 0.20^{\circ} \\ &\quad 0, \cdots 0 \\ &12.1rpm, 1173.7rpm\} \end{aligned} \tag{76}$$

Now, linearizing eq. (39) around the equilibrium point (76) yields the linear state space model:

$$\dot{x} = Ax + Bu \tag{77}$$

Considering the LQR cost function upon the model (77) as:

$$\begin{gathered} J = \frac{1}{2}\left(X_f^T S_f X_f\right) + \frac{1}{2}\int_{t_0}^{t_f}\left(X^T QX + U^T RU\right)dt \\ S_f, Q \geq 0, R > 0 \end{gathered} \tag{78}$$

results in the optimal state feedback control action $u = -kx$ and thus,

$$\dot{x} = (A - Bk)x \tag{79}$$

In the wind turbine plant of this article, the zero final point weight S_f yields the following concise form of:

$$J = \int\left(x^T Qx + u^T Ru\right)dt \tag{80}$$

Regarding the limits of actuator size and cost, the following values of weighting matrices R and Q are used:

$$\begin{gathered} Q = 0.001c^T c \\ R = \begin{bmatrix} 100 & & \\ & 100 & \\ & & 100 \end{bmatrix} \# \end{gathered} \tag{81}$$

where the observation matrix c is obtained according to the output measurement arrangement:

$$y = cx = [x_1 x_2 x_3]^T \tag{82}$$

the Kalman gain matrix k is obtained by:

$$k = R^{-1} B^T P \tag{83}$$

in which, the PDM P is obtained through solving the algebraic Riccati matrix equation as:

$$A^T P + PA - PBR^{-1} B^T P + Q = 0 \tag{84}$$

Now, the results of applying the above-explained LQR on the wind turbine are revealed in Figs. 16 through 18.

Furthermore, the comparison of statistical mean of tracking errors between the adaptive RBFNN and the LQR control systems in Figs. 19 and 20 clarifies the significant tracking capability of the newly designed method.

To evaluate the effect of measurement noises on the performance of proposed RBFNN control system, white noise strings of zero mean and unity standard deviation are added on measurement signals. In Figs. 21 through 26, the deteriorations due to noisy measurements on tracking errors of the RBFNN system are compared with the noise-free RBFNN control system. Unlike the LQR weakness against measurement noises, negligible differences are observed between the RBFNNs system with and without noise effects. In fact, the deterioration of states about 0.1% of tracking error of the noise free situation makes the adaptive RBFNN a superior control system for the floating wind turbines. For a better comparison, in Table 1, the mean and standard deviation of tracking state variables with and without noise on the measurement signals of the RBFNN control systems are compared with the LQR. The small standard deviation in comparison to LQR proves the superiority of the adaptive RBFNN controller even against noises.

4. Conclusion

The RBFNN controller, through its adaptive and robust structure, leads to increase the system robustness and stability against uncertainties and stochastic noises. Filtering undesired noises and uncertainties in input actions by providing error dynamics in an integral form holds the finite horizon tracking error around zero. Direct Lyapunov based design of the proposed control system guarantees its stability proof. Through wide-range Figures and tabulated results, the comparison of the intelligent RBFNN method together with the classical LQR system with respect to the reference wind turbine model not affected by uncertainties, revealed the tracking accuracy of the RBFNN method. Owing to compensation of the uncertainties through radial basis approximation, the superiority of RBFNN with respect to LQR is vivid, though more design parameters of NN as initial weights and biases require more test data of the under-control system. According to Table 1, the comparison of statistical mean of tracking errors along state trajectories show many times reduction of errors through implementation of the adaptive RBFNN system. The little values of tacking errors even in the presence of uncertainties and noises validate the RBFNN control system as a trustworthy reference system for future research works.

Declaration of Competing Interest

The authors declare that they have no known competing financial interests or personal relationships that could have appeared to influence the work reported in this paper.

References

[1] Homer JR. Physics-based control-oriented modelling for floating offshore wind turbines. M.S. thesis, Univ. British Columbia, Vancouver, BC, Canada; 2015.
[2] Christiansen S, Knudsen T, Bak T. Extended onshore control of a floating wind turbine with wave disturbance reduction. The Science of Making Torque from Wind; 2012.
[3] Namik H, Stol K, Jonkman J. State-space control of tower motion for deepwater floating offshore wind turbines. Proceedings of the 46th AIAA Aerospace Sciences Meeting and Exhibit. 2008.
[4] Ni YQ, Chen Y, Ko JM, Kao DQ. Neuro-control of cable vibration using semi-active magnetorheological dampers. Eng Struct 2002;24(3):295–307.
[5] Shiraishi T, Nakaya N, Morishita S. Vibration control of structure equipped with MR damper using neural network. Dyna Des Conf 2001;8:1748–52.
[6] Zhang TP, Ge SS. Adaptive dynamic surface control of nonlinear systems with unknown dead zone in pure feedback form. Automatica 2008;44(7):1895–903.
[7] Song B, Hedrick JK. Dynamic Surface Control of Uncertain Nonlinear Systems: An LMI Approach. Communications and Control Engineering, Springer London.
[8] Zhou L, Fei S, Jiang C. Adaptive integral dynamic surface control based on fully tuned radial basis function neural network. J Syst Eng Electron 2010;21(6):1072–8.
[9] Butt WA, Yan L, Amezquita KS. Adaptive integral dynamic surface control of a hypersonic flight vehicle. Int J Syst Sci 2015;46(10):1717–28.
[10] Shtessel Y, Edwards C, Fridman L, Levant A. Sliding Mode Control and Observation. Control Engineering, Springer New York.
[11] Tahoun AH. Time-varying multiplicative/additive faults compensation in both actuators and sensors simultaneously for nonlinear systems via robust sliding mode control scheme. J Franklin Inst 2019;356(1):103–28.
[12] Qi W, Zong G, Karimi HR. Sliding mode control for nonlinear stochastic semi-Markov switching systems with application to space robot manipulator model. IEEE Trans Ind Electron 2019.
[13] Xinghuo Yu, Zhihong M. Fast terminal sliding-mode control design for nonlinear dynamical systems. IEEE Trans Circ Syst I: Fundam Theory Appl 2002;49(2):261–4.
[14] Boukattaya M, Mezghani N, Damak T. Adaptive non-singular fast terminal sliding-mode control for the tracking problem of uncertain dynamical systems. ISA Trans 2018;77:1–19.
[15] Keighobadi J, Yarmohammadi MJ. New chatter free sliding mode synchronization of steer by wire system under chaotic condition. J Mech Sci Technol 2016;30:3829–34.
[16] Ahmed S, Wang H, Tian Y. Model-free control using time delay estimation and fractional-order non-singular fast terminal sliding mode for uncertain lower-limb exoskeleton. J Vib Control 2018;24(22):5273–90.

[17] Lewis FL, Jagannathan S, Ye¸sildirek A. Neural network control of robot manipulators and nonlinear systems, The Taylor & Francis systems and control book series. London: Taylor & Francis; 1999.

[18] Shi Z, et al. Artificial intelligence techniques for stability analysis and control in smart grids: Methodologies, applications, challenges and future directions. Appl Energy 2020.

[19] Sun T, Pei H, Pan Y, Zhou H, Zhang C. Neural network-based sliding mode adaptive control for robot manipulators. Neurocomputing 2011;74(14–15):2377–84.

[20] Tran Minh, Kang Hee-Jun. Adaptive Terminal Sliding Mode Control of Uncertain Robotic Manipulators Based on Local Approximation of a Dynamic System. Neurocomputing 2016. https://doi.org/10.1016/j.neucom.2016.09.089.

[21] Zhou Qi, Zhao S, Li H, Lu R, Wu C. Adaptive neural network tracking control for robotic manipulators with dead zone. IEEE Trans Neural Netw Learning Syst 2019; 30(12):3611–20.

[22] Liu C, Zhao Z, Wen G. Adaptive neural network control with optimalnumber of hidden nodes for trajectory tracking of robot manipulators. Neurocomputing 2019; 350:136–45.

[23] Prasad LB, Singh KP, Javvaji HL. Simulation of neuro-fuzzy position controller for induction motor drive using Simulink. In: Proceedings of XXXI National Systems Conference, MIT Manipal, India; 2007.

[24] Keighobadi J, Hosseini-Pishrobat M, Faraji J. Adaptive neural dynamic surface control of mechanical systems using integral terminal sliding mode. Neurocomputing 2019;379:141–51.